ADVANCED FUNCTIONAL MATERIALS
www.afm-journal.de

Materials Views
www.MaterialsViews.com

FULL PAPER

Eliminating the Trade-Off between the Throughput and Pattern Quality of Sub-15 nm Directed Self-Assembly via Warm Solvent Annealing

*Jong Min Kim, YongJoo Kim, Woon Ik Park, Yoon Hyung Hur, Jae Won Jeong, Dong Min Sim, Kwang Min Baek, Jung Hye Lee, Mi-Jeong Kim, and Yeon Sik Jung**

The directed self-assembly (DSA) of block copolymers (BCPs) has been suggested as a promising nanofabrication solution. However, further improvements of both the pattern quality and manufacturability remain as critical challenges. Although the use of BCPs with a high Flory-Huggins interaction parameter (χ) has been suggested as a potential solution, this practical self-assembly route has yet to be developed due to their extremely slow self-assembly kinetics. In this study, it is reported that warm solvent annealing (WSA) in a controlled environment can markedly improve both the self-assembly kinetics and pattern quality. A means of avoiding the undesirable trade-off between the quality and formation throughput of the self-assembled patterns, which is a dilemma which arises when using the conventional solvent vapor treatment, is suggested. As a demonstration, the formation of well-defined 13-nm-wide self-assembled patterns (3σ line edge roughness of ≈2.50 nm) in treatment times of 0.5 min (for 360-nm-wide templates) is shown. Self-consistent field theory (SCFT) simulation results are provided to elucidate the mechanism of the pattern quality improvement realized by WSA.

1. Introduction

The directed self-assembly (DSA) of block copolymers (BCPs) is expected to be a low-cost and high-yield technical route to complement the resolution limit of photolithography.[1–11] The secure registrations of BCP microdomains in lithographically defined templates can achieve the multiplication of the pattern density by a few to tens of times.[6,7,11,12] Remaining challenges related to DSA include further reductions of the defect density (<0.01 cm^{-2}), minimizing the size (<10 nm), and reducing the edge roughness (<8% of line width).[13] Both traditional thermodynamic theories and recent self-consistent simulation results predict that the use of BCPs with a higher Flory-Huggins interaction parameter (χ),[14] a measure of the degree of incompatibility between two blocks, is one of the key strategies to resolve these challenges. Poly(styrene-*b*-ethylene oxide) (PS-*b*-PEO),[8] poly(styrene-*b*-dimethylsiloxane) (PS-*b*-PDMS),[15,16] poly(2-vinylpyridine-*b*-dimethylsiloxane) (P2VP-*b*-PDMS),[17] polyhedral oligomeric silsesquioxane (POSS) containing BCPs,[18,19] poly(*N*-xyloglucooligosaccharide-*b*-para-trimethylsilylstyrene) (XGO-*b*-PTMSS),[20] and poly(trimethylsilylstyrene-*b*-D,L-lactide) (PTMSS-*b*-PLA) have been suggested as examples of high-χ BCPs. However, the use of high-χ BCPs is also associated with technical issues, as follows: 1) the difficulty of achieving a perpendicular alignment with respect to the substrate surface, and 2) the significant slow-down of self-assembly kinetics, affecting the aspect ratio and throughput.

The first issue stems from the inevitable significant difference in the surface-free energy between two polymer blocks in high-χ BCPs. Many previous studies showed that the use of appropriate solvent annealing conditions can enable perpendicular alignment by directional solvent evaporation.[21,22] Recently, Willson et al. demonstrated that the application of a polarity-switchable top-coat layer can provide a neutral interface for both blocks and uniformly achieve the perpendicular alignment of a low-molecular-weight BCP.[23] On the other hand, the use of a cylindrical morphology for the formation of line/space patterns can serve as an alternative to circumvent this issue despite the concomitant relatively low aspect ratio.[4,5,24,25] Si-containing BCPs[15–17,26–30] can be used as a robust etch mask to enhance the aspect ratio via pattern-transfer to the underlying resist.

The kinetic issue is caused by the exponential decrease of the interdiffusivity of polymer chains as a function of the segregation strength (χN), where N is the degree of polymerization.[31] Typically, the rate-limiting step during the defect removal process during BCP self-assembly is the diffusion of polymer chains through the interface (i.e., interdiffusion), which is especially slow for high-χN BCPs. A thermal annealing treatment, which is simple, convenient, and highly effective for

J. M. Kim, Y. Kim, W. I. Park, Y. H. Hur, J. W. Jeong, D. M. Sim, K. M. Baek, J. H. Lee, Prof. Y. S. Jung
Department of Materials Science and Engineering
Korea Advanced Institute of Science and Technology
291 Daehak-ro, Yuseong-gu
Daejeon 305–701, Republic of Korea
E-mail: ysjung@kaist.ac.kr

Dr. M.-J. Kim
Samsung Advanced Institute of Technology (SAIT)
Mt. 14–1, Nongseo-dong, Giheung-gu
Yongin-si, Gyeonggi-do 446–712, Republic of Korea

DOI: 10.1002/adfm.201401529

the assembly of low-χ BCPs (e.g., poly(styrene-*b*-methylmethacrylate)(PS-*b*-PMMA)) or low-*N* BCPs, often results in poorly ordered morphologies for high-χN BCPs[17,29,30] if *N* is not sufficiently small. It is well known that this constraint can be mitigated by solvent annealing due to its far better effectiveness as regards the facilitation of BCP chain diffusion. Nonetheless, solvent annealing for strongly segregated BCPs typically requires an assembly time of a few to even tens of hours, resulting in an insufficient throughput of pattern formation.[15,17] Recently, Buriak and co-workers reported considerably faster alignment of BCPs through a combination of microwave heating and solvent annealing.[32] Moreover, Morris et al. reported microwave annealing for rapid pattern formation without the use of a solvent.[33] We also previously demonstrated the ultrafast formation of low-*N* (forming sub-10 nm patterns) PS-*b*-PDMS BCP patterns via the low-temperature thermal assistance to solvent annealing.[30,34] Ryu et al. found that two-step annealing consisting of solvent and thermal treatments is highly effective for the assembly of high-*N* BCPs.[35] Ross and co-workers also reported a significant reduction of the assembly time of BCPs on densely guided narrow trench templates by rapidly increasing the substrate temperature following a conventional room-temperature solvent annealing process.[36] However, the rapid, one-step assembly of long-range ordering of high-χN BCPs on micrometer-scale wide templates, obtainable by low-cost photolithography, has yet to be demonstrated.

Furthermore, despite the improvements in the self-assembly kinetics, relatively little attention has been paid to the effects of the annealing parameters on the DSA pattern quality based on high-χ BCPs. The line edge roughness (LER) and line width roughness (LWR) are widely used as useful measures of the lithography pattern quality, which directly influences the performances of semiconductor device.[37–39] For example, the leakage current of sub-100 nm MOS transistors significantly increases with the LWR.[37] Along this line, ITRS (International Technology Roadmap for Semiconductors) requires that the 3σ roughness should be below a pattern width of 8%, which is a stringent requirement for DSA and other emerging lithography solutions.[13] Although the remediation of line edge roughness by DSA was successfully demonstrated by Stoykovich and Nealey,[40] the LER and LWR of low-χ BCPs are typically larger than those of the target. To reduce the pattern roughness effectively, the width of the intermixing layer between two polymer blocks should be reduced by the use of high-χ BCPs. Using calculations based on a phase-field model, Patrone et al. recently predicted, to achieve an LER below 1 nm, that a BCP with a larger χ by several fold would be required.[41] However, thus far, there has been no systematic study to reveal the dependence of the high-χ DSA pattern quality on solvent-based treatment parameters.

Here, we report that warm solvent annealing (WSA) performed at 40–60 °C can simultaneously achieve both a significant improvement in the pattern formation kinetics as well as improvements in the pattern quality of BCPs with a high segregation strength ($\chi N \approx 128$ at RT). We employed a solvent annealing system equipped with multiple temperature-feedback controllers and an in situ swelling ratio monitoring device. While there is a trade-off effect between the pattern formation time and the edge roughness for conventional room-temperature solvent annealing (RTSA) as a function of the swelling ratio (SR) of BCP thin film, we found that WSA shows a considerably shorter pattern formation time ($t_{\min} \approx 3$ min for 1-µm-wide templates with $t_{\min}$ equal to approximately 0.5 min for 360-nm-wide templates) as well as a lower LER (≈2.5 nm), which are highly superior to those ($t_{\min} \approx 10$ min for 1-µm-wide templates, corresponding to an LER of approximately 4.5 nm) of conventional solvent annealing with the same BCP. To the best of our knowledge, no previous study has reported that solvent vapor annealing at a slightly elevated temperature can markedly reduce the roughness of patterns despite the inevitable decrease of effective χ. Although the conventional prediction is that a lower effective χ would cause a relatively diffuse interface between two blocks and the degradation of pattern quality, the new findings in this study are contrary to such expectations. On the basis of a self-consistent field theory (SCFT) simulation, the smaller LER associated with WSA is explained by the relatively small internal stress and consequently less deformation of the microdomains during the last stage of solvent evaporation.

2. Results and Discussion

Figure 1a schematically describes the solvent annealing chamber system, which has a bottom receptacle and an upper lid. The chamber was designed for independent and precise control of the temperatures of the solvent (T_{sol}), BCP sample (T_{sub}), and upper lid (T_{lid}). Three independent heating modules enable precise control of the temperatures. Even though we can control the temperature of both the solvent and sample independently, we fixed the temperature of the sample (T_{sub}) to be the same as the temperature of the solvent (T_{sol}) during the WSA process. Although SR can be controlled using different T_{sub} and T_{sol}, SR responded too sensitively to the difference between these two temperatures. For example, if T_{sol} is slightly higher than T_{sub}, the solvent vapor can condense to a liquid on the BCP films. A similar phenomenon was already reported in our previous research.[34] On the other hand, if T_{sub} is slightly higher than T_{sol}, the SR significantly decreases, resulting in insufficient chain mobility. Thus, maintaining the condition of $T_{\text{sol}} = T_{\text{sub}}$ and controlling the amount of solvent in the bottom chamber were more advantageous for precise control of SR and to achieve high-quality patterns. A flexible silicon rubber heater is used to maintain a slightly and uniformly higher T_{lid} than T_{sol} during the annealing process. In this way, we were able to prevent the solvent from condensing on the bottom lid and on the quartz plate for the maintenance of a constant vapor pressure in the chamber.

The transparent quartz plate was used as a feed-though to optically measure the swelling ratio (SR) of the BCP film. Thin film reflectometry (F20-UV, Filmetrics Inc.) was used to in situ measure the reflectance spectra and to calculate the thickness of dry and swollen BCP films. SR values were obtained by dividing the swollen thickness by the initial thickness. Also, keeping the same temperature (*T*) for both the BCP sample and the solvent prevents solvent vapor condensation on the BCP films. The leakage holes in the chamber can play a role in preventing filling of the chamber with saturated vapor. To obtain precise controllability of SR in a wide range, we adjusted the amount of solvent in the chamber rather than changing

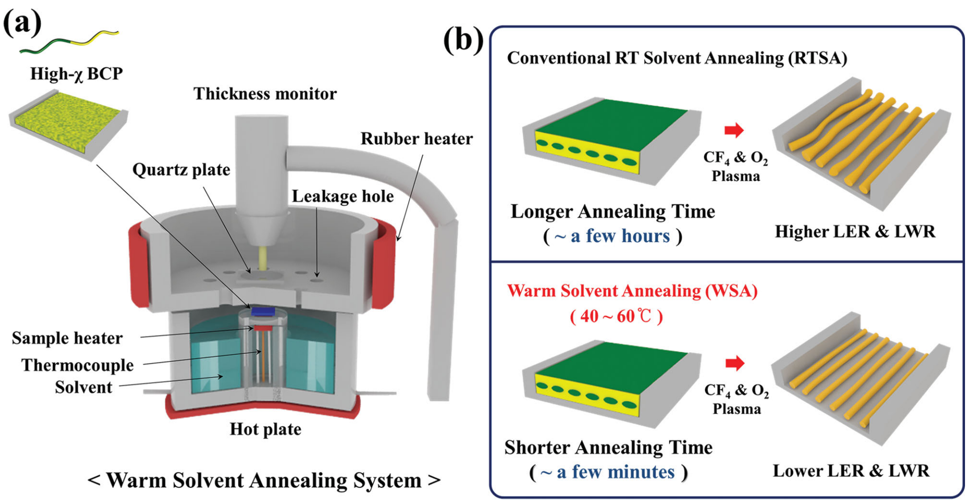

Figure 1. Schematic illustrations of directed self-assembly induced by warm solvent annealing. a) Structure of the treatment chamber system equipped with three independent temperature controllers and heaters. The swelling ratio (SR) of the BCP films was in situ monitored using an optical thickness measurement tool. b) Schematic comparison of the self-assembled pattern quality depending on the assembly temperature.

the number of leakage holes. Slow solvent removal after self-assembly can affect the domain spacing of BCPs and lateral ordering of the BCP microdomains, and thus we used a rapid (<1 s) quenching process to freeze-in the BCP morphology. While the rapid removal of solvent from annealed BCP samples are equally important for RTSA and WSA, the higher temperature of WSA would lead to faster evaporation of solvent and expedite the quenching process.

We adopted an SR range from 1.7 to 2.3 for SD45K BCP. If SR is lower than 1.7, the self-assembly kinetics is too slow to induce ordering of the patterns. On the contrary, if the swelling ratio is higher than 2.3, partial dewetting of the BCP films is observed due to BCP film instability. In these experiments, we mainly used toluene (solubility parameter, $\delta = 18.3$ MPa$^{1/2}$),[42] which is a good solvent for the majority of PS ($\delta = 18.5$ MPa$^{1/2}$) blocks. We chose PS-*b*-PDMS at 45 kg mol^{-1} (SD45) as a model high-χN (≈128 at RT) BCP system, which requires at least several hours for self-assembly via conventional RT solvent annealing. Figure 1b schematically compares the self-assembled pattern formation results for the RTSA and WSA treatments, showing a clear difference in the roughness depending on SR and T. These results will be discussed in detail based on experimental data as well as theoretical models.

Figures 2a–d show the time evolution of BCP patterns assembled with different temperatures and SR conditions. The measured pitch (L_0) and line width (= critical dimension; CD) values

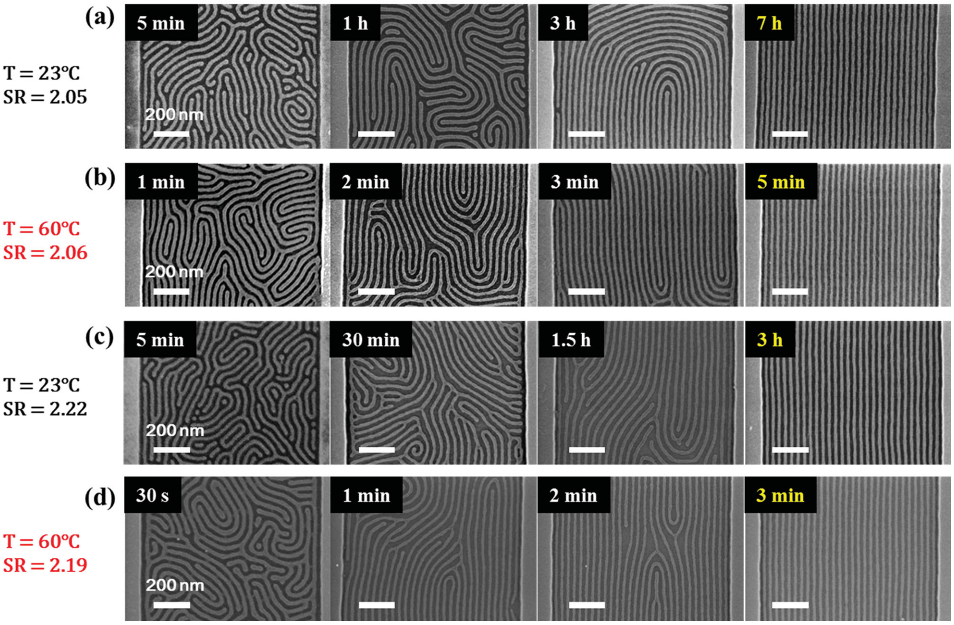

Figure 2. Solvent-annealed morphologies of a PS-*b*-PDMS BCP depending on the temperature, swelling ratio (SR), and time. Warm solvent annealing (WSA) at 60 °C achieved markedly faster assembly than a RT treatment with a comparable SR.

were between 34–38 nm and 12–17 nm, respectively. As we previously reported, the CD of the pattern derived from high-χ BCPs is strongly affected by the SR.[17] This causes a decrease in the CD with an increase of the SR due to the interfacial screening effect caused by the incorporated solvent molecules, resulting in a decrease of the effective χ-parameter (χ_{eff}).[43,44] The decrease of L_0 and CD with an increase of the SR, which follows the relationship of $L_0 \sim \chi_{\text{eff}}^{1/6}$,[14] was previously reported for the same PS-*b*-PDMS BCP.[27] Recently, Russell and co-workers confirmed similar phenomenon using in situ grazing-incidence small-angle X-ray scattering (GISAXS).[45] For a similar SR (2.05–2.06), the required annealing times for RT and 60 °C treatments were 420 min (7 h) and 5 min, respectively, showing the marked effectiveness of the thermal assistance in solvent annealing in terms of its ability to prevent defects. A higher SR (2.19) for the 60 °C treatment further shortened the assembly time to 3 min. **Figure 3**b shows the change in the defect density depending on the annealing conditions. To measure the defect density, we used an image analysis tool for SEM images. This method has already been reported in previous studies regarding DSA defects.[32,35] For line/space patterns, typical examples of self-assembly defects are dots, junctions, dislocations, and terminal points. According to a power law, the defect density (ρ) of self-assembled BCP patterns as a function of the assembly time (t) can be expressed as $\rho \sim t^{-\nu}$, where ν is the empirical kinetic exponent. The kinetic exponent (ν) of RTSA was calculated to be 0.63, 0.84, 1.01, and 1.67 at SRs of 1.75, 2.05, 2.22, and 2.30, while those for WSA were 2.15 and 2.97 at SR 2.06 and 2.19, respectively, indicating that the defect density decreases much more rapidly with an increase in T_{sub} ($=T_{\text{sol}}$) and SR. These results confirm that the adoption of WSA is highly effective for throughput enhancement during the DSA pattern formation process.

Although there is a relatively small change in absolute temperature between WSA and RTSA, their self-assembly kinetics was strikingly different, as mentioned above. The thermally induced improvement of the self-assembly kinetics for the high-χ BCP can be attributed to two major factors: 1) the faster swelling dynamics of the BCP film resulting from the faster evaporation of solvent molecules from the solvent (source) and their gas-phase transport and diffusion in BCP films and 2) increased chain diffusivity of BCPs due to the thermal activation effect during the polymer interdiffusion process. First, the more rapid BCP swelling can be experimentally confirmed by monitoring the swelling kinetics. Using optical reflectometry, we measured the time-dependent SRs of BCP films under various conditions. The SR was adjusted (by changing the empty volume in the chamber) between 1.70 and 2.30, which was found to be appropriate for the assembly of the SD45 BCP. While the saturation SR (2.20) took approximately 1000 s for RTSA, the 60 °C warm treatment arrived at a similar saturation swelling level (2.19) within only 100 s, as shown in Figure 3a. This can be understood from the exponentially increasing evaporation rate of the solvent as a function of the temperature. Faster swelling reduces the time-delay for the initiation of the assembly process, during which the BCP chains organize promptly. For example, the assembly at 60°C is complete even before the time to reach the saturation swelling state at RT. However, the much faster swelling rate alone cannot explain the enhanced self-assembly kinetics. The RT assembly process required orders-of-magnitude longer treatment times (>400 min) after the saturation swelling point, whereas WSA took only few minutes of additional treatment time, indicating the significant effectiveness of thermal activation for defect removal. It should be noted that the best WSA results were obtained for a high SR of >2. The high concentration of solvent in the BCP would significantly lower the activation energy barrier compared to dry BCPs and may be associated with the marked improvement of self-assembly kinetics despite the small change of temperature. On the other hand, the upper boundary of the assembly temperature at the high SR was set by the instability of the BCP films. We observed that a T_{sub} value higher than 80 °C at an SR of ≈2.2 led to the dewetting of the film. For the normal WSA operating ranges, however, there was no dewetting of the BCP films due to stringent management of the process parameters in our chamber system.

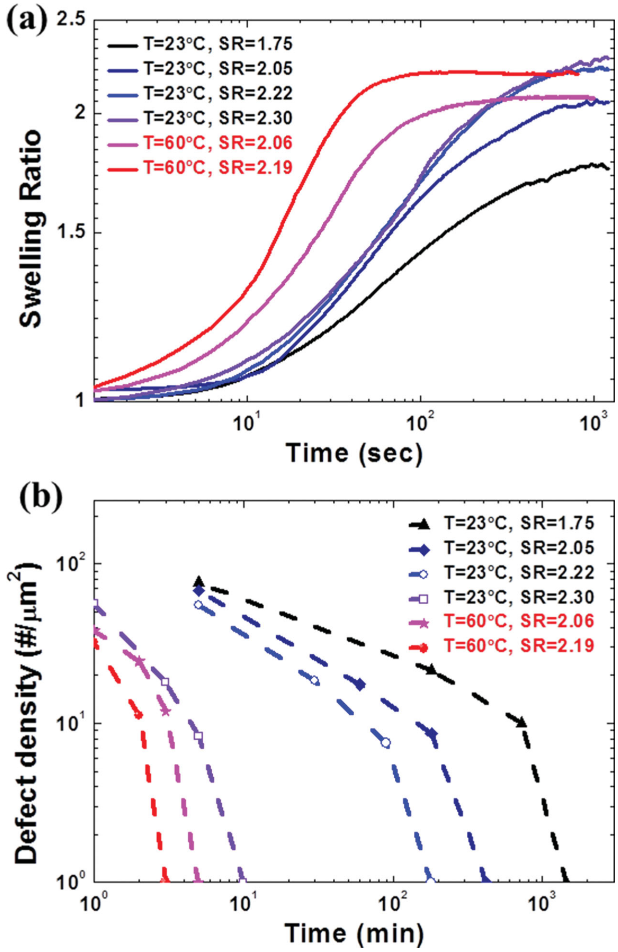

Figure 3. Comparison of a) swelling dynamics and b) self-assembly kinetics of a PS-*b*-PDMS BCP for RTSA and WSA. a) Swelling ratio as a function of the treatment time and temperature. b) Time-trace of defect density. The BCPs treated with WSA show much faster swelling and decay times of defect densities.

Figure 4a shows a low-magnification SEM image of patterns assembled with an SR of 2.19 and with T_{sub} = 60 °C. These settings constitute the condition that maximizes the

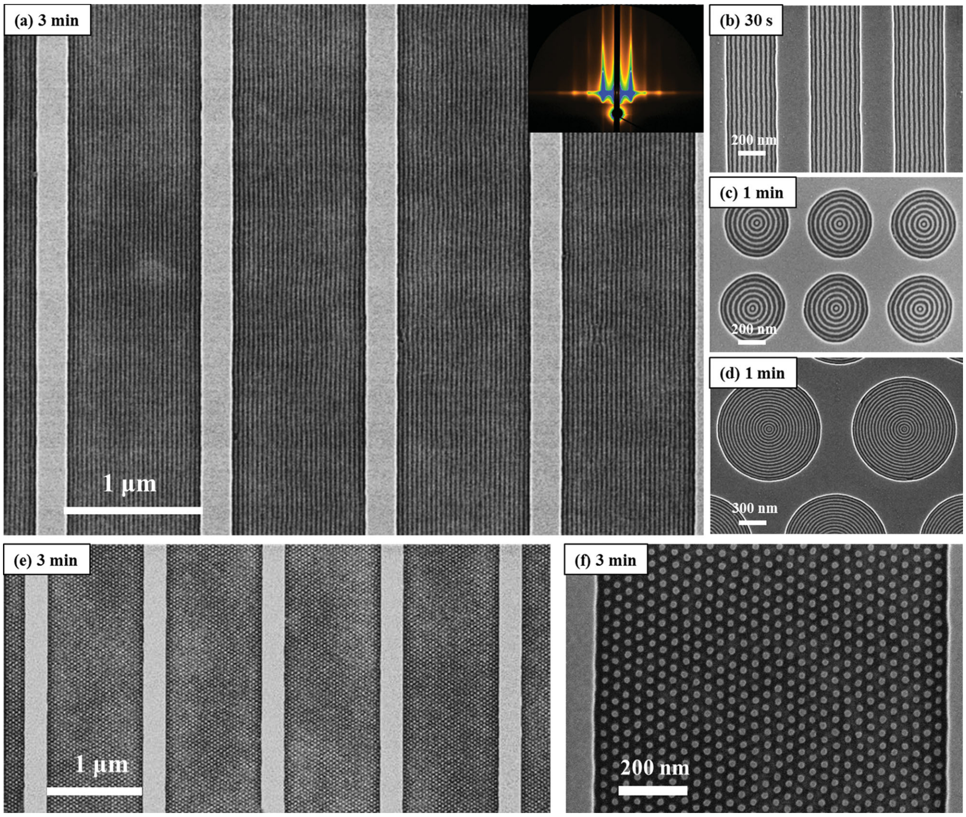

Figure 4. Ultrafast assembly of cylindrical patterns in various trench templates via WSA (*T* = 60 °C, SR = 2.19). a) A low-magnification SEM image of line patterns generated with 1-µm-wide trench templates in 3 min. The inset shows the corresponding GISAXS pattern. b) Self-assembled patterns assembled in a relatively narrow trench (width = 360 nm) at 30 s. c,d) The assembly was also successful with circular trenches. e) Low- and f) high-magnification SEM images of sphere-forming BCP patterns assembled via WSA.

DSA throughput without compromising the degree of uniformity. The assembly time could be shortened even more to 30 s by reducing the dimension of the template width further to 360 nm, as shown in Figure 4b. The assembly condition was also effective for circular trench templates, which induce the generation of circular patterns (Figure 4c,d) and for sphere-forming PS-*b*-PDMS (MW = 56 kg/mol, Figure 4e,f). It should be noted that the extremely short assembly time of 30 s is even shorter than the saturation time of the BCP swelling ratio.

We now discuss how thermal assistance to solvent annealing process can also improve the quality of the patterns in addition to the self-assembly kinetics. **Figure 5**a,b shows high-magnification SEM images of patterns assembled at RT (with SR = 2.30) and at 60 °C (SR = 2.19), respectively. The two samples were prepared using the conditions that maximize the assembly kinetics without causing dewetting at the different assembly temperatures and while ensuring that the two samples have the same line width of 12.1 nm. The superior pattern quality of the 60 °C-annealed sample, as shown in the SEM images, is quantitatively substantiated by the 44% and 48% smaller LER (2.50 nm) and LWR (3.12 nm) values. This tendency was also noted in the comparisons of the patterns shown in Figure 5c,d, which have comparable line widths of 13.6 nm and 13.3 nm, respectively. **Figure 6** represents the power spectral density (PSD) analysis results, which provide the information related to how the roughness determined at each spatial frequency contributes to the overall roughness. The lower power spectral density (PSD) values over all frequencies between 3 and 850 µm^{-1} for the WSA samples (Figure 6a,b) quantitatively confirm the superiority of WSA in terms of pattern quality. This tendency was also consistent for the 40 °C-annealed samples. Especially, the low frequency roughness of WSA always shows the much lower than that of RTSA. This will be explained the following SCFT simulation results.

Figure 7 present the dependence of the pitch, LER, and LWR values on SR and CD. For the RT treatment, the LER and LWR increased with an increase in SR (and with a decrease in CD due to the decreasing trend of CD as SR increased, as mentioned above and as shown in Figure 7a). Thus, for RTSA, there is a clear trade-off between the assembly time and pattern quality, as shown in **Figure 8**. For example, boosting the self-assembly kinetics (assembly time ≈ 10 min) by increasing the SR to 2.30 inevitably increased the LER to 4.49 nm, and the achievement of small LER of 2.50 nm under a low SR of 1.75 required a prolonged assembly time that exceeded 1000 min.

In contrast, for WSA, low roughness values were maintained nearly continually regardless of the SR when it was between 1.70 and 2.19, indicating that a high throughput of pattern formation can be obtained without compromising the pattern quality, as shown in Figure 8. Thus, simultaneous minimization of both the assembly time (3 min for a 1-µm-wide template and 30 s for a 360-nm-wide template) and roughness

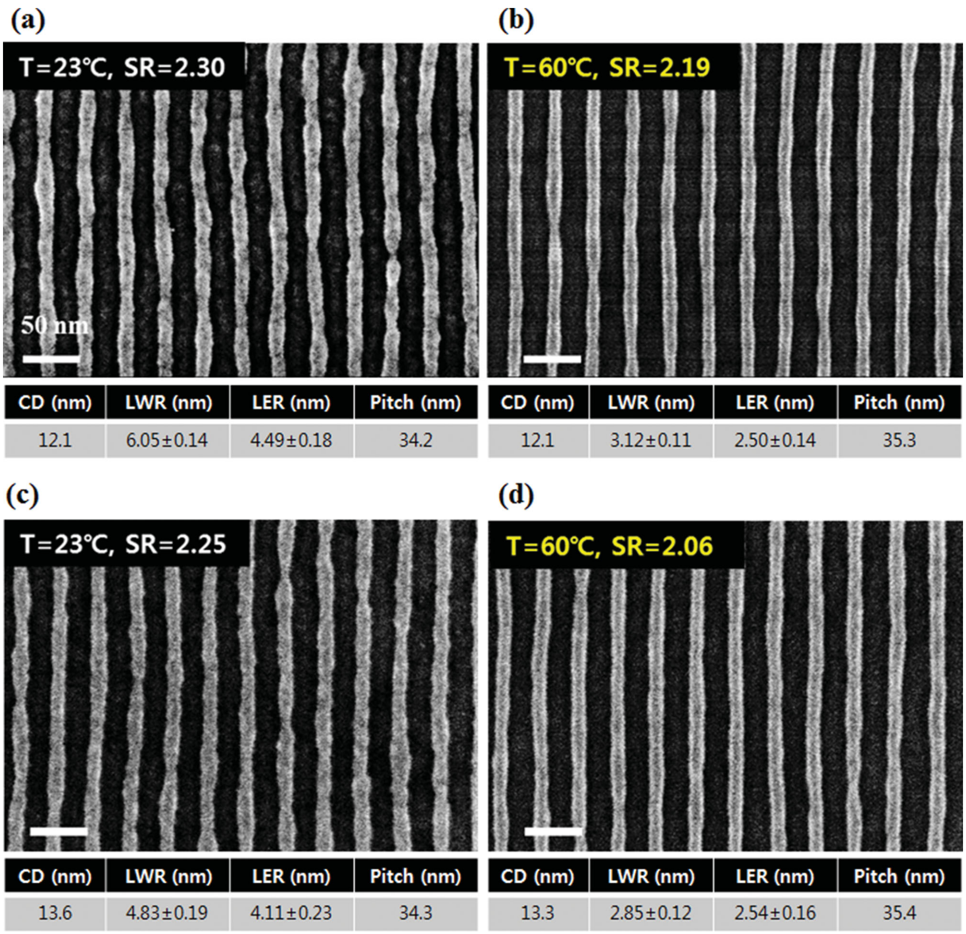

(a)

CD (nm)	LWR (nm)	LER (nm)	Pitch (nm)
12.1	6.05±0.14	4.49±0.18	34.2

(b)

CD (nm)	LWR (nm)	LER (nm)	Pitch (nm)
12.1	3.12±0.11	2.50±0.14	35.3

(c)

CD (nm)	LWR (nm)	LER (nm)	Pitch (nm)
13.6	4.83±0.19	4.11±0.23	34.3

(d)

CD (nm)	LWR (nm)	LER (nm)	Pitch (nm)
13.3	2.85±0.12	2.54±0.16	35.4

Figure 5. Superior pattern quality obtained by WSA. a,b) High-magnification SEM images of the 12-nm-wide cylinder patterns prepared by RTSA and WSA, respectively. c,d) Comparison of the 13-nm-wide patterns.

(LER ≈ 2.50 nm; LWR ≈ 3.12 nm) is achieved by increasing the solvent annealing temperature. We also tested the use of other solvents with similar δ with toluene such as tetrahydrofuran (THF, $\delta = 18.5$ MPa$^{1/2}$) and propylene glycol monomethyl ether acetate (PGMEA, $\delta = 18.2$ MPa$^{1/2}$) for both spin-casting and WSA. As Figure S1 in the Supporting Information demonstrates, similar rapid self-assembly was achieved using THF (30 s) and PGMEA (3 min). Although we suppose that further optimization is needed for improvement of pattern quality, we can conclude from these preliminary results that these CMOS-process-compatible solvents have sufficient potential to replace toluene for both spin-casting and WSA.

However, the result of mostly lower LER and LWR values for the 60 °C WSA treatment compared to the RT treatment is not consistent with the above-mentioned calculated results that predicted a decrease in the roughness values with an increase in the χ-parameter because, for the same SR, a BCP at a higher temperature would have a smaller effective χ value. This discrepancy demands a theoretical analysis that can more realistically reflect the physical situation of solvent annealing—especially its nonequilibrium nature during and after solvent evaporation from BCPs. Evaporation of the solvent from a BCP sample abruptly and significantly reduces the volume of BCP films along the vertical direction while the external and internal structures along the in-plane directions are preserved, resulting in the shrinkage of the film thickness and a geometrical change in the microdomains only along the vertical direction, as was experimentally confirmed by Ober and co-workers.[46] The value of χ_{eff} also increases with a decrease in SR, eventually recovering to a dry value.

Thus, we used a SCFT calculation able to reflect changes of the film thickness, shape-deformation, and effective χ parameter ($\chi_{\mathrm{eff}}N$) to investigate their effects on the quality of the patterns. The SCFT study in this article focuses on the effects of $\chi_{\mathrm{eff}}N$ and thickness shrinkage on the long-range interfacial fluctuation at the "final quenched state" after solvent evaporation, and can explain why the roughness of pattern is very sensitive to a relatively small change of absolute temperature of solvent vapor annealing. At a high SR, self-assembly is induced with a lower effective χ; as a result, the system is governed by a lower $\chi_{\mathrm{eff}}N$ than bulk BCPs. To estimate the $\chi_{\mathrm{eff}}N$ values, we used the equation of the effective Flory-Huggins interaction parameter based on the screening effect ($\chi_{\mathrm{eff}} = \chi(1 - f_s)$, f_s = the volume fraction of solvent in the BCP films) and the temperature of BCPs. For an SR of 2.20, the estimated $\chi_{\mathrm{eff}}N$ values were approximately 0.33 χN at RT and 0.29 χN at 60 °C. However, when the system is rapidly quenched with the removal of the solvent from the BCP films, the swollen film thickness

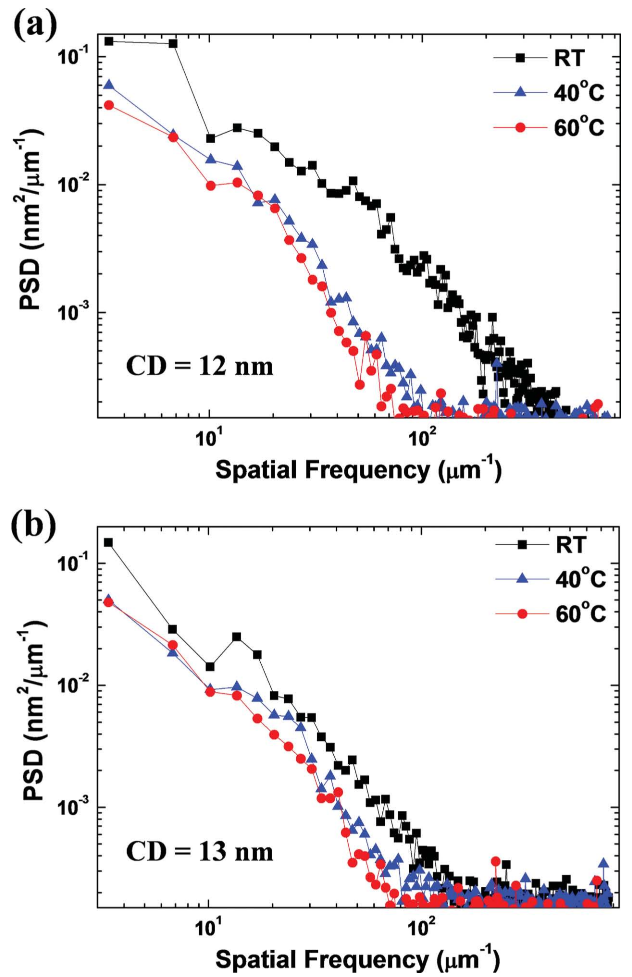

Figure 6. Power spectral density (PSD) functions depending on the assembly temperature. For the line patterns with a) CD = 12 nm and b) = 13 nm.

returns to the as-spun thickness. At the very last stage of the quenching process, due to the remaining solvent molecules, polymer chains can still be slightly mobile and locally redistributed under a higher $\chi_{\mathrm{eff}}N$ compared to that in the fully swollen state, causing the deformation of microdomains and an increase in the degree of interfacial fluctuations. At this stage (almost dried film), the WSA process has a lower $\chi_{\mathrm{eff}}N$ than in the RTSA process due to the elevated temperature. We simplified the dynamic status of solvent annealing to three steps: 1) solvent annealing at a constant SR, 2) rapid volume shrinkage along the thickness direction, and 3) a rearrangement of polymer chains under an increased χN. **Figure 9** shows simulation snapshots of these steps for both the RTSA and the WSA process. The initial (swollen) state of the system is modeled using RTSA with $\chi_{\mathrm{eff}}N = 40$ at RT and WSA with $\chi_{\mathrm{eff}}N = 35$ at 60 °C with an optimized box size to represent a fully relaxed state of the swollen film (Figure 9a). The quenched morphology is then obtained by compressing the system in the z-direction while redistributing all field values, resulting in an elliptical cross-sectional shape of the cylinders, as shown in Figure 9b. After being quenched, the polymer chains are locally rearranged with a higher $\chi_{\mathrm{eff}}N$. For this specific case, we modeled RTSA with $\chi_{\mathrm{eff}}N = 100$ and WSA with $\chi_{\mathrm{eff}}N = 85$, considering the reciprocal dependence of χ on T. The solvent in the BCP film was rapidly removed by opening the lid of the chamber system, during which the temperature of the BCP sample was maintained by the feedback temperature controller.

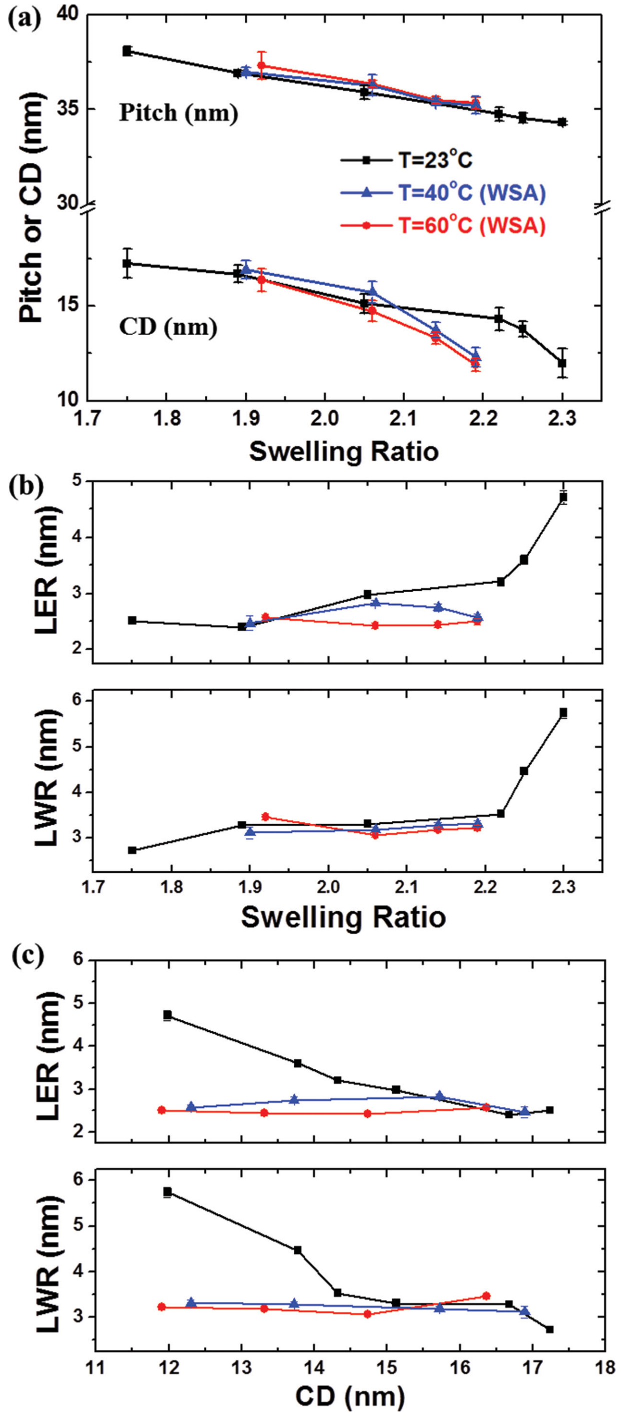

Figure 7. Quantitative characteristics of the generated self-assembly patterns. Measurements of a) the CD (critical dimension) and pitch and b) the LER and LWR as obtained for different swelling ratios and assembly temperatures. c) The LER and LWR are plotted as a function of CD for comparison.

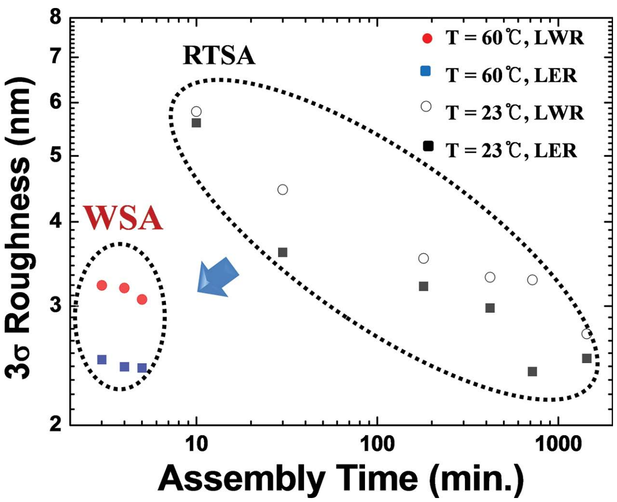

Figure 8. Map of the pattern quality and assembly time depending on the solvent annealing temperatures. WSA can achieve both lower roughness (better pattern quality) and a shorter assembly time.

During the rearrangement process, the elliptical shapes of the cylinders are partially deformed due to the incommensurate thickness of the quenched film (the dry thickness of the BCP film is much thinner than that in the swollen state under dynamic equilibrium). For the RTSA process, due to the high χN in the dry state, a highly compressed cylinder in the z-direction and a flat interface between the top PDMS and PS layer produce a high stress field near the interface of the cylinder. As a result, relatively large fluctuation at the interface of the cylinder and greater lateral undulation of the cylinder patterns were observed in the calculated result, as described in Figure 9c. However, for WSA, due to the smaller χN, a lower stress field resulted from the weaker compression along the z-direction, achieving a smaller LER and LWR compared to the conventional RTSA process. These results can explain the big difference of low frequency roughness between the WSA and RTSA in Figure 6. The much higher PSD values of low frequency for RTSA indicate the relatively larger degree of deformation during solvent evaporation compared to WSA.

Because the sample with CD = 12 nm had a higher SR than that of the sample with CD = 13 nm, the degree of roughness reduction using warm SVA is comparatively much more pronounced. In other words, although the pattern quality of the final patterns is comparable for the WSA patterns with CD = 12 and 13 nm, the RTSA pattern quality is relatively worse in the case of CD = 12 nm due to more deformation caused by a higher SR. Therefore, our experimental results are well consistent with SCFT simulation results.

3. Conclusions

In conclusion, we suggested a warm solvent annealing treatment as a practical route which simultaneously improves the pattern quality and throughput of the directed self-assembly process based on a high-χN BCP. We experimentally demonstrate that solvent annealing at an elevated temperature (60 °C) can eliminate the inevitable trade-off between the self-assembly kinetics and the edge fluctuations which arise during conventional room-temperature solvent annealing.

We also conducted a modeling study based on self-consistent field theory to suggest that edge fluctuation of solvent-annealed patterns can be caused by the deformation of microdomains resulting from internal stress after most of the solvent molecules are removed. In contrast, in the case of warm solvent annealing, the degree of interfacial deformation was found to be reduced due to the lower effective χ-parameter after drying,

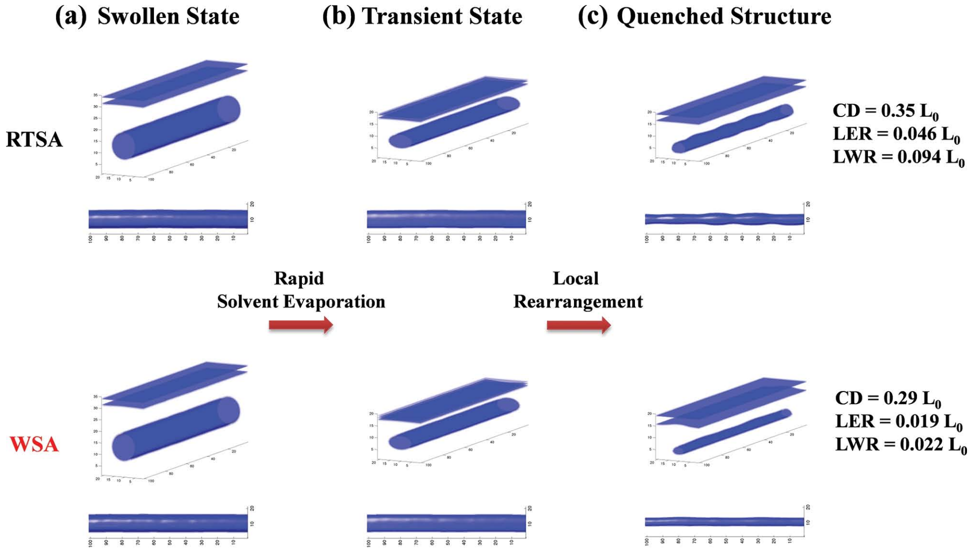

Figure 9. SCFT simulation. Side-tilt and top-down snapshot images of calculated self-assembly structures for different steps and annealing conditions. a) Swollen state, b) transient state at a later stage of solvent evaporation, and c) quenched morphology after the complete evaporation of the solvents. The calculated deformation degree of the microdomains and the interfacial fluctuations were significantly smaller for WSA as compared to RTSA.

achieving superior pattern quality. We expect that this approach can contribute to the development of more reliable and practical nanolithography solutions.

4. Experimental Section

Block Copolymer (BCP) Self-Assembly: PS-*b*-PDMS BCPS with MWs of 45 kg/mol (SD45) and 56 kg/mol (SD56) and a hydroxyl-terminated PS homopolymer with a MW of 38 kg/mol were purchased from Polymer Source Inc. (Canada). The toluene solutions of the hydroxyl-terminated PS homopolymer (1.5 wt%), SD45 (≈0.8–1.2 wt%) and SD56 (0.9 wt%) were prepared and used for the formation of monolayer cylindrical microdomains. The thickness of the BCP films was optimized in a range of 30–35 nm depending on the swelling ratio. For the directed self-assembly (DSA) of BCPs, Si trench templates with a periodicity of 1 um and a depth of 40 nm were fabricated using KrF photolithography followed by reactive ion etching. The hydroxyl-terminated PS homopolymer solution was spin-coated on the Si substrate and thermal annealed at 150 °C for 1.5 h. The brush-coated Si substrate was then washed with toluene to remove unattached polymer chains. Before starting the WSA treatment, the chamber system was already in a state of thermal equilibrium ($T_{sol} = T_{sub} = T_{lid}$) and this was confirmed by employing multiple feedback controllers in real time. After filling the chamber with solvent vapor, we opened the upper lid and put the sample in the chamber and immediately closed the upper lid. After the annealing process, we rapidly opened the chamber, after which the solvent molecules in the BCP film were immediately evaporated.

Plasma Oxidation: After the self-assembly process, the samples were etched by CF_4 plasma (50W, 21 s, 15 mTorr) to remove the top-segregated PDMS, followed by O_2 plasma (60W, 30 s, 15 mTorr) to remove the PS matrix to obtain well-defined SiO_x line patterns (lateral dimensions, 12–17 nm).

Characterization: During the self-assembly process, the thicknesses of the BCP films were in situ monitored by a thin film reflectometry tool (F20-UV, Filmetrics Inc.) by measuring the reflectance spectra. The self-assembled morphologies were investigated by field emission scanning electron microscopy (FE-SEM: Hitachi S-4800) with an acceleration voltage of 15 kV and a working distance of 4.5 mm. For the quantitative analyses of the critical dimension (CD), pitch, line width roughness (LWR), and line edge roughness (LER) using the SEM images, commercial image analysis software (SuMMIT) was used.

Self-Consistent Field Theoretic (SCFT) Simulation: The cylinder phase of block copolymers having appropriate brush layers (modeled with light particles attracted to one of the blocks) was simulated through a hybrid particle-field simulation method developed by Fredrickson et al.[47] To obtain the cylinder phase, block copolymers with a minority volume fraction of 30% were compressed to thin films with thicknesses comparable to those in the experimental data. The top PDMS brush and bottom PS brush successfully mimicked the experimental PDMS-air interface and PS brush on the Si substrate, respectively. Simulations were performed using the newly developed lattice Boltzmann diffusion equation solver optimized for graphics processing units (GPUs).[48]

Supporting Information

Supporting Information is available from the Wiley Online Library or from the author.

Acknowledgements

This work was supported by the Basic Science Research Program (NRF-2013R1A1A2061440) and by the MOTIE (Ministry of Trade, Industry & Energy (10048504) and KSRC (Korea Semiconductor Research Consortium) support program for the development of the future semiconductor device. The authors also acknowledge Pohang Accelerator Laboratory for grazing-incidence small-angle X-ray scattering (GISAXS) measurements.

Received: May 12, 2014
Revised: October 14, 2014

[1] R. A. Segalman, H. Yokoyama, E. J. Kramer, *Adv. Mater.* **2001**, *13*, 1152.
[2] S. O. Kim, H. H. Solak, M. P. Stoykovich, N. J. Ferrier, J. J. de Pablo, P. F. Nealey, *Nature* **2003**, *424*, 411.
[3] J. Y. Cheng, A. M. Mayes, C. A. Ross, *Nat. Mater.* **2004**, *3*, 823.
[4] C. T. Black, R. Ruiz, G. Breyta, J. Y. Cheng, M. E. Colburn, K. W. Guarini, H. C. Kim, Y. Zhang, *IBM J. Res. Dev.* **2007**, *51*, 605.
[5] S. B. Darling, *Prog. Polym. Sci.* **2007**, *32*, 1152.
[6] I. Bita, J. K. Yang, Y. S. Jung, C. A. Ross, E. L. Thomas, K. K. Berggren, *Science* **2008**, *321*, 939.
[7] R. Ruiz, H. M. Kang, F. A. Detcheverry, E. Dobisz, D. S. Kercher, T. R. Albrecht, J. J. de Pablo, P. F. Nealey, *Science* **2008**, *321*, 936.
[8] S. Park, D. H. Lee, J. Xu, B. Kim, S. W. Hong, U. Jeong, T. Xu, T. P. Russell, *Science* **2009**, *323*, 1030.
[9] R. A. Segalman, *Mater. Sci. Eng. R-Rep.* **2005**, *48*, 191.
[10] M. P. Stoykovich, M. Muller, S. O. Kim, H. H. Solak, E. W. Edwards, J. J. de Pablo, P. F. Nealey, *Science* **2005**, *308*, 1442.
[11] J. Y. Cheng, C. T. Rettner, D. P. Sanders, H.-C. Kim, W. D. Hinsberg, *Adv. Mater.* **2008**, *20*, 3155.
[12] J. Y. Cheng, D. P. Sanders, H. D. Truong, S. Harrer, A. Friz, S. Holmes, M. Colburn, W. D. Hinsberg, *ACS Nano* **2010**, *4*, 4815.
[13] The International Technology Roadmap for Semiconductors. http://www.itrs.net (accessed 2014).
[14] F. S. Bates, G. H. Fredrickson, *Ann. Rev. Phys. Chem.* **1990**, *41*, 525.
[15] Y. S. Jung, C. A. Ross, *Nano Lett.* **2007**, *7*, 2046.
[16] Y. S. Jung, J. B. Chang, E. Verploegen, K. K. Berggren, C. A. Ross, *Nano Lett.* **2010**, *10*, 1000.
[17] J. W. Jeong, W. I. Park, M. J. Kim, C. A. Ross, Y. S. Jung, *Nano Lett.* **2011**, *11*, 4095.
[18] T. Hirai, M. Leolukman, S. Jin, R. Goseki, Y. Ishida, M. A. Kakimoto, T. Hayakawa, M. Ree, P. Gopalan, *Macromolecules* **2009**, *42*, 8835.
[19] T. Hirai, M. Leolukman, C. C. Liu, E. Han, Y. J. Kim, Y. Ishida, T. Hayakawa, M. Kakimoto, P. F. Nealey, P. Gopalan, *Adv. Mater.* **2009**, *21*, 4334.
[20] J. D. Cushen, I. Otsuka, C. M. Bates, S. Halila, S. Fort, C. Rochas, J. A. Easley, E. L. Rausch, A. Thio, R. Borsali, C. G. Willson, C. J. Ellison, *ACS Nano* **2012**, *6*, 3424.
[21] S. H. Kim, M. J. Misner, T. Xu, M. Kimura, T. P. Russell, *Adv. Mater.* **2004**, *16*, 226.
[22] J. Bang, B. J. Kim, G. E. Stein, T. P. Russell, X. Li, J. Wang, E. J. Kramer, C. J. Hawker, *Macromolecules* **2007**, *40*, 7019.
[23] C. M. Bates, T. Seshimo, M. J. Maher, W. J. Durand, J. D. Cushen, L. M. Dean, G. Blachut, C. J. Ellison, C. G. Willson, *Science* **2012**, *338*, 775.
[24] C. T. Black, O. Bezencenet, *IEEE Trans. Nanotechnol.* **2004**, *3*, 412.
[25] D. Sundrani, S. B. Darling, S. J. Sibener, *Langmuir* **2004**, *20*, 5091.
[26] Y. S. Jung, W. Jung, C. A. Ross, *Nano Lett.* **2008**, *8*, 2975.
[27] Y. S. Jung, C. A. Ross, *Adv. Mater.* **2009**, *21*, 2540.
[28] Y. S. Jung, J. H. Lee, J. Y. Lee, C. A. Ross, *Nano Lett.* **2010**, *10*, 3722.
[29] K. W. Gotrik, A. F. Hannon, J. G. Son, B. Keller, A. Alexander-Katz, C. A. Ross, *ACS Nano* **2012**, *6*, 8052.
[30] W. I. Park, K. Kim, H.-I. Jang, J. W. Jeong, J. M. Kim, J. Choi, J. H. Park, Y. S. Jung, *Small* **2012**, *8*, 3762.
[31] T. P. Lodge, M. C. Dalvi, *Phys. Rev. Lett.* **1995**, *75*, 657.

[32] X. Zhang, K. D. Harris, N. L. Wu, J. N. Murphy, J. M. Buriak, *ACS Nano* **2010**, *4*, 7021.
[33] D. Borah, R. Senthamaraikannan, S. Rasappa, B. Kosmala, J. D. Holmes, M. A. Morris, *ACS Nano* **2013**, *7*, 6583.
[34] J. W. Jeong, Y. H. Hur, H.-j. Kim, J. M. Kim, W. I. Park, M. J. Kim, B. J. Kim, Y. S. Jung, *ACS Nano* **2013**, *7*, 6747.
[35] E. Kim, H. Ahn, S. Park, H. Lee, M. Lee, S. Lee, T. Kim, E.-A. Kwak, J. H. Lee, X. Lei, J. Huh, J. Bang, B. Lee, D. Y. Ryu, *ACS Nano* **2013**, *7*, 1952.
[36] K. W. Gotrik, C. A. Ross, *Nano Lett.* **2013**, *13*, 5117.
[37] H. W. Kim, J. Y. Lee, J. Shin, S. G. Woo, H. K. Cho, J. T. Moon, *IEEE Trans. Electron. Devices* **2004**, *51*, 1984.
[38] W. Steinhogl, G. Schindler, G. Steinlesberger, M. Traving, M. Engelhardt, *Microelectron. Eng.* **2004**, *76*, 126.
[39] A. Asenov, S. Kaya, A. R. Brown, *IEEE Trans. Electron. Devices* **2003**, *50*, 1254.
[40] M. P. Stoykovich, K. C. Daoulas, M. Muller, H. M. Kang, J. J. de Pablo, P. F. Nealey, *Macromolecules* **2010**, *43*, 2334.
[41] P. N. Patrone, G. M. Gallatin, *Macromolecules* **2012**, *45*, 9507.
[42] A. F. Barton, *CRC Handbook of Solubility Parameters and Other Cohesion Parameters* CRC Press, Boca Raton, FL **1991**.
[43] E. Helfand, Y. Tagami, *J. Polym. Sci. Part B: Polym. Phys.* **1996**, *34*, 1947.
[44] T. Hashimoto, M. Shibayama, H. Kawai, *Macromolecules* **1983**, *16*, 1093.
[45] X. Gu, I. Gunkel, A. Hexemer, W. Gu, T. P. Russell, *Adv. Mater.* **2014**, *26*, 273.
[46] M. Y. Paik, J. K. Bosworth, D. M. Smilges, E. L. Schwartz, X. Andre, C. K. Ober, *Macromolecules* **2010**, *43*, 4253.
[47] S. W. Sides, B. J. Kim, E. J. Kramer, G. H. Fredrickson, *Phys Rev Lett* **2006**, 96.
[48] H. Chen, Y. Kim, A. Alexander-Katz, *J. Chem. Phys.* **2013**, 138.